Flight photon counting electron multiplying charge coupled device development for the Roman Space Telescope coronagraph instrument

Flight photon counting electron multiplying charge coupled device development for the Roman Space Telescope coronagraph instrument

Patrick Morrissey,[a,*] **Leon Harding**,[b] **Nathan Bush**,[a,c] **Michael Bottom**,[d] **Bijan Nemati**,[e] **Andrew Daniel**,[a] **Bongim Jun**,[f] **Luz Maria Sierra Martinez**,[a] **Niyati Desai**,[g] **Dave Barry**,[h] **Rhonda-Topaz Davis**,[h] **Richard Demers**,[i] **David Hall**,[c] **Andrew Holland**,[c] **Pete Turner**,[h] **and Brian Shortt**[j]

[a]Jet Propulsion Laboratory, California Institute of Technology, Pasadena, California, United States
[b]Virginia Tech National Security Institute, Arlington, Virginia, United States
[c]Open University, Centre for Electronic Imaging, Milton Keynes, United Kingdom
[d]University of Hawaii at Manoa, Institute for Astronomy, Hilo, Hawaii, United States
[e]Tellus1 Scientific, LLC, Madison, Alabama, United States
[f]Northrup Grumman Mission Systems, Woodland Hills, California, United States
[g]California Institute of Technology, Pasadena, California, United States
[h]Teledyne-e2v, Chelmsford, United Kingdom
[i]GMTO Corporation, Pasadena, California, United States
[j]European Space Research and Technology Center, Noordwijk, The Netherlands

Abstract. We describe the development of flight electron multiplying charge coupled devices (EMCCDs) for the photon-counting camera system of a coronagraph instrument (CGI) to be flown on the 2.4-m Nancy Grace Roman Space Telescope. Roman is a NASA flagship mission that will study dark energy and dark matter, and search for exoplanets with a planned launch in the mid-2020s. The CGI is intended to demonstrate technologies required for high-contrast imaging and spectroscopy of exoplanets, such as high-speed wavefront sensing and pointing control, adaptive optics with deformable mirrors, and ultralow noise signal detection with photon counting, visible-sensitive (350 to 950 nm) detectors. The camera system is at the heart of these demonstrations and is required to sense both faint and bright targets ($10^{-4} - 10^{7}$ counts-s^{-1}) adaptively at up to 1000 frames-s^{-1} to provide the necessary feedback to the instrument control loops. The system includes two identical cameras, one to demonstrate faint light scientific capability, and the other to provide high-speed real-time sensing of instrument pointing disturbances. Our program at the Jet Propulsion Laboratory (Pasadena, California, United States) has evaluated the low-signal performance of radiation-damaged commercial EMCCD sensors and used those measurements as a basis for targeted radiation hardening modifications developed in partnership with the Open University (Milton Keynes, United Kingdom) and Teledyne-e2v (Chelmsford, United Kingdom). A pair of EMCCDs with test features was then developed and their low signal performance is reported here. The program has resulted in the development of a flight version of the EMCCD with low signal performance improved by more than a factor of three over the commercial one after exposure to 2.6×10^{9} protons-cm^{-2} (10 MeV equivalent). The flight EMCCD sensors are contributed by ESA through a contract with Teledyne-e2v (Chelmsford, United Kingdom). We will describe the program requirements, sensor design, test results and metrics used to evaluate photon counting performance. [DOI: 10.1117/1.JATIS.9.1.016003]

Keywords: coronagraph; charge coupled device; electron multiplying charge coupled device; instrumentation; photon counting; detector; camera.

Paper 22101G received Oct. 16, 2022; accepted for publication Feb. 14, 2023; published online Mar. 19, 2023.

*Address all correspondence to Patrick Morrissey, patrick.morrissey@jpl.nasa.gov

1 Introduction

The NASA Jet Propulsion Laboratory (JPL) is developing a coronagraph instrument (CGI) for the 2.4 m Nancy Grace Roman Space Telescope, expected to launch in the mid-2020s. The CGI will demonstrate technologies needed for direct imaging and spectroscopy of exoplanets.[1] To meet the challenges of detecting the faint planet signal, JPL selected the electron multiplying charge coupled device (EMCCD) from Teledyne-e2v (Chelmsford, United Kingdom) as part of a previous study.[2] To streamline the instrument development, a single camera design serves two broadly different applications. The two cameras are arranged on each side of a coronagraph mask that is used to reject the core of bright light from the stellar target while admitting the nearby field containing possible planetary orbits. A science camera downstream of the mask called ExCam (the exoplanetary systems camera) is used to acquire stars, to provide feedback to the adaptive optical system required to reduce diffracted light close to a stellar image, and to collect the remaining faint light from target objects in the field. The second camera upstream of the mask is used for high-speed pointing. This camera, called LoCam (the low order wavefront sensing camera), collects the bright rejected starlight from the coronagraph reimaged as a pupil in a 50×50 pixel region that is read out at 1000 frames-s^{-1}. Both cameras are required to read out at high speed (although not at high frame rate) to support shutterless operation, and to operate over a wide range of intensity ($\sim 10^8$x for ExCam).

The camera system is designed around a Teledyne-e2v CCD201 that has been customized to improve performance in the environment of space. The general features and capability of the CCD201 are well described in the literature.[3,4] The sensor provides adjustable gain for photon counting operation, which eliminates the contribution of read noise for faint targets while providing the dual advantages of silicon quantum efficiency (QE) and compatibility with bright light operations that are fundamental to coronagraphic operations. While the CGI EMCCDs are "thin" devices with peak sensitivity at 600 nm, it would be possible to use the same technology in a thicker and more red sensitive EMCCD.

This paper describes our program to develop a flight EMCCD sensor design for CGI. We have evaluated the irradiated performance of the commercial CCD201 in collaboration with the centre for electronic imaging (CEI) of the Open University (Milton Keynes, United Kingdom). The commercial version of the sensor is found to be sensitive to radiation exposure in the single kRad range and must be shielded from potentially damaging solar events. The key effects of the radiation damage are to increase dark current, and to reduce the sensitivity of the detector disproportionately to faint light, effects that are also observed in damaged CCDs on the Hubble Space Telescope.[5] The gain register is also found to saturate in response to energetic particle detections, which has the effect of producing tails on cosmic ray tracks that obscure the underlying data and raise the background level. While the cosmic ray rate is a manageable 1 cm^{-2}-min^{-1} at sea level, it is predicted to be up to 5 cm^{-2}-s^{-1} in the L2 environment outside the Earth's magnetic field. This rate would be a limiting factor for long exposures given the $\sim$1.9 cm^2 active area of the sensor.

Under contract with JPL and in collaboration with CEI, Teledyne-e2v has designed and produced a pair of modified versions of the CCD201 with test features intended to mitigate radiation damage and cosmic ray tails. These test sensors, the CCD301 and CCD302, have been irradiated with flight-like doses of protons at the Loma Linda University Medical Center (Loma Linda, California, United States). The program has demonstrated substantial improvements in performance over the commercial design, and select features from the CCD301 and CCD302 have been incorporated into a ruggedized flight version called the CCD311. Flight sensors of this design were delivered to JPL by Teledyne-e2v in late 2021 through a contribution from ESA. These sensors have been integrated into the flight camera systems and are currently under test.

The outline of this paper is as follows. In Sec. 2, we describe the camera system requirements. In Sec. 3, we describe the impact of the space environment on EMCCD performance. In Sec. 4, we describe our evaluation of the commercial EMCCD and devices modified for improved performance in flight. Finally, in Sec. 5, we summarize our results and expected improvements with selected modifications to the commercial EMCCD design.

Table 1 Detection goals for the Roman CGI camera system.

Parameter	Flux	Time
Imaging detection	0.063 photons-px^{-1}-s^{-1}	3 min
Spectroscopy detection	0.002 photons-px^{-1}-s^{-1}	6 hrs

2 Requirements

The coronagraph is a NASA technology demonstration, which means that it is funded chiefly to demonstrate new technologies that could reduce risk for future missions by providing a platform not only to advance the state of the art but also to provide a real-world test of the elements together as a system. The CGI is advancing the technical state of the art in several areas, including deformable mirror technology, masks, detectors, and algorithms.[6] Some requirements (and goals), such as lifetime are based on the anticipated future needs of NASA exoplanetary missions.[7–9] Models of coronagraph performance[10] place challenging detection goals on the EMCCD. The most recent CGI estimated flux levels are shown in Table 1 (personal communication, B. Nemati).

The goal flux levels are quite faint, particularly for spectroscopy, and drive the need for ultra-low noise that can be achieved with the EMCCD in photon counting mode. As we will show, the ability to meet these requirements in the space environment is principally what separates the flight from the commercial EMCCD designs. CGI is designed for operation at L2, ~1.5 million kilometers from Earth and well outside its protective magnetic field and belts of trapped radiation. As a result, the detectors will be exposed to energetic protons in the form of a steady stream of galactic cosmic rays (GCRs) with energies typically greater than 100 MeV,[11] and sporadic large pulses of protons from solar flares with energies typically <100 MeV.[12] The GCR are sufficiently energetic that they cannot be shielded within the weight constraints of the instrument, and they are treated as a persistent but manageable observational nuisance. Sporadic solar flares arrive with a log-normal intensity distribution primarily in the seven years around solar maximum, next predicted in 2025. The total radiation exposure over the mission can be dominated by a small number of large flares.[13] Since this is the case, the cameras are designed to a conservative standard for which there is a 95% confidence that the dose in flight will not exceed the test level.

The key flight EMCCD requirements for the Roman CGI are listed in Table 2 and meet the needs of both the ExCam and LoCam in spite of their widely different applications. Programmable on-chip gain in concert with an appropriate discriminator threshold enables zero read noise in the photon counting mode, intermediate gain for low noise (but not noiseless) pointing, and unity gain for bright light imaging. In both applications, pixels are read at 10 MHz, but the LoCam reads only a small 50×50 region to achieve the required 1000 frames-s^{-1}. Several of the performance parameters are impacted by the response of the EMCCD to the space radiation environment, and a complete evaluation requires an in-depth treatment of a quantity called "detective" QE (dQE) specific to the EMCCD.

Table 2 references the three key noise sources that combined with QE determine the detection threshold of the camera. Read noise and clock-induced charge (CIC) are noise sources added to the data during each frame readout, while dark current is generated continuously in the detector silicon. As an example, consider a 6-hr observation comprised of 120-s individual frames of data. The total dark current would be (for the 95% pixel) 9.9 counts-pixel^{-1} with an additional 1.8 counts-pixel^{-1} of CIC and thus a noise of $\sqrt{9.9 + 1.8} = 3.4$ counts-pixel^{-1} and a detection threshold of $5 \times 3.4 = 17$ counts-pixel^{-1}, compared to an expected signal of 43 photons in the same interval. It is apparent that the elimination of read noise is essential to make the detection possible, and also that the dQE needs to be sufficiently high ($\geq 17/43$) to convert the photon signal. This conversion efficiency is the subject of the next section.

Table 2 Key requirements for the Roman CGI camera system.

Parameter	Requirement
Lifetime	>21 months (goal >5.25 years)
QE	>0.85 electrons-photon^{-1} @580 nm
CIC	<0.010 counts-px^{-1}-frames^{-1}
Dark (95%)	<1.65 counts-px^{-1}-hour^{-1}
Read noise (unity gain)	<200 electrons
Read noise (photon counting)	0 electrons
Gain	1 to 7500*x*
Pixel rate	>10 MHz
LoCam latency	<1 ms
LoCam frame rate	>1000 frames-s^{-1}
Full well (image)	>50,000 electrons
Full well (serial)	>90,000 electrons

3 Photon Counting Considerations

The efficiency of a detector is typically reported in terms of its QE, the number of photoelectrons or packets of electrons created per incident photon. When detector noise is not dominant, QE is often the most important characteristic. An EMCCD in unity gain mode exhibits QE characteristics typical of a conventional silicon CCD. The additional application of a high field (35 to 50 V) in the EMCCD gain register amplifies single electrons (or packets of electrons) into pulses that are much larger than the camera read noise, even at a 10-MHz pixel rate. This enables the transition from direct measurement of photoelectrons to the measurement of individual signal pulses from the gain register, and has a significant impact on what would in practice be deemed as the true end-to-end efficiency. Read noise, which is injected into the signal after the EMCCD gain register, is essentially eliminated by virtue of an appropriate pulse counting threshold. For detector-limited, faint light observations, the signal-to-noise ratio (SNR) thus achieved with gain can be much higher than is possible by raising the QE. This trade is often made in photon counting systems faced with signals that would otherwise be invisible in the face of a limiting detector background.

To quantify the end-to-end efficiency of an EMCCD in photon counting mode, one must consider not only the QE of the electron-generating silicon, but also a set of efficiency factors that enable (or prevent) those electrons from being detected. The combined product of the QE with each of the identified factors defines an effective or detective QE (dQE). We consider the effects of the detector pulse height distribution (PHD), coincidence, cosmic rays, and radiation damage effects in our analysis to arrive at an estimate of the true sensitivity of the EMCCD in a mission implementation. We account for these effects with a set of efficiency factors that are introduced in the following expression:

$$\mathrm{dQE} = \mathrm{QE} \times (\epsilon_{\mathrm{PC}}\epsilon_{\mathrm{CO}}\epsilon_{\mathrm{CR}}) \times (\epsilon_{\mathrm{CC}}\epsilon_{\mathrm{HP}}), \tag{1}$$

where ϵ_{PC} is the photon counting efficiency factor, ϵ_{CO} is the coincidence efficiency factor, ϵ_{CR} is the cosmic ray efficiency factor, ϵ_{CC} is the charge collection efficiency factor, and ϵ_{HP} is the hot pixel efficiency factor representing the fraction of pixels that meet the dark current requirements. The last pair of factors will vary over the life of the mission as the detector is exposed to radiation. In this section we describe the origin of each of these factors and their impact on the dQE of the photon counting EMCCD.

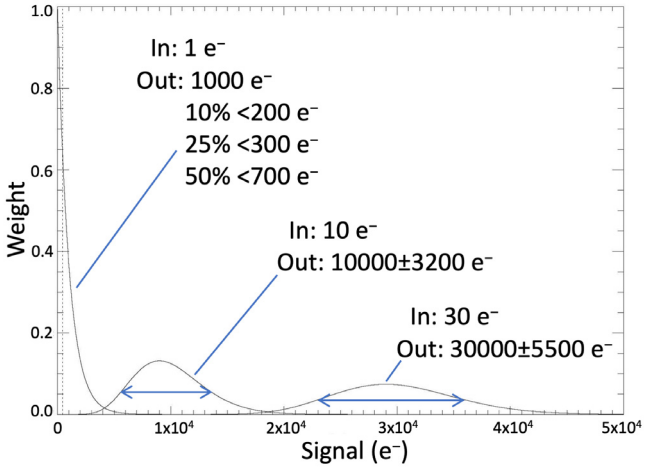

Fig. 1 Three theoretical PHDs for an EMCCD with 604 multiplication elements operating at a gain of 1000× with 1, 3, and 10 electron input. The simulation does not include shot noise in the input signal.

3.1 *Pulse Height Distribution and Signal Losses Due to Camera Noise*

The statistical output of the EMCCD gain register is a function of the operating gain and the number of input electrons.[14] We refer to the probability distribution of output electrons from the register as the PHD, an example of which is shown in Fig. 1 for 1, 3, and 10 electron inputs to the gain register operating at a mean gain of 1000. Single electron input to the gain register results in an exponential output distribution, while multiple electron input results in a broad gaussian-shaped profile. The profile introduces a noise factor[15] (the "excess noise factor") that reduces the SNR by a factor of $\sqrt{2}$ for signals originating prior to the gain register. One can think of this ("analog") mode of operation effectively halving the QE of a conventional CCD operating at unity gain, albeit with much lower effective noise (which could result in higher SNR depending on the circumstance). The excess noise factor is eliminated in the photon counting limit of low signal levels when it can be assured that there will not be more than one signal electron in an image pixel in a given frame. In this limiting scenario, the "brightness" of a pulse measured from the gain register has no correlation with the actual brightness of the source due to the exponential PHD. It is the frequency of pulses measured from a given detector location provides this information.

The exponential nature of the photon counting EMCCD PHD has the consequence that some fraction of events are hidden by read noise, and the gain must be chosen to minimize this fraction while balancing the impact of high gain on other performance parameters, such as charge transfer efficiency. The gain is chosen to be the minimum value that meets the photon counting efficiency requirements. The magnitude of the read noise therefore defines the gain that is required to detect a sufficiently large fraction of events. For Roman CGI, we require at least 90% of events to have a signal level at the output of the gain register that is greater than five times the read noise. This ensures high detection efficiency while reducing the possibility of detecting spurious read noise events to near zero. One could experiment with lower thresholds as a means of reducing the required gain as long as leakage of other noise sources above the threshold level remains negligible. The required gain is determined from the exponential PHD for single electron input to the EMCCD gain register[14]

$$\mathrm{PHD}(x) = e^{-x/g}/g, \tag{2}$$

where x is the output of the serial gain register and g is the mean gain. An example of a measured PHD is shown in Fig. 2.

The photon counting efficiency factor ϵ_{PC} is the probability that any pulse from the EMCCD gain register will have an amplitude greater than a specified threshold t. This quantity is the integral of Eq. (2) for $x > t$, or

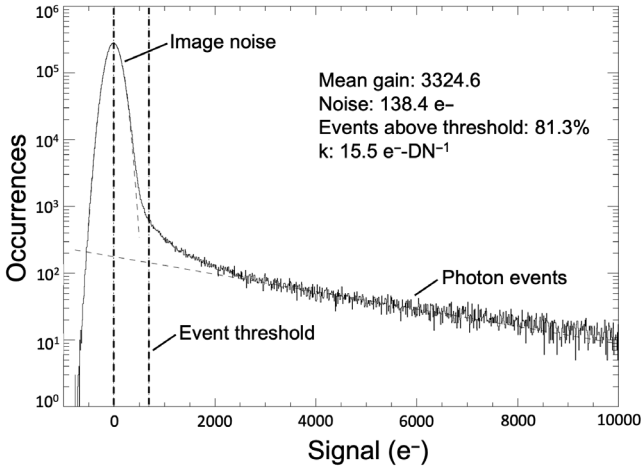

Fig. 2 A measured PHD from a CCD201 with 604 multiplication elements operating at a gain of 3300×. The histogram shows the distribution of values measured in the image, and it can be seen that since most pixels have no signal that the gaussian read noise dominates at low signal levels. The plot includes a fit to the read noise and the extrapolated distribution of amplified events. The vertical dashed line shows the 5σ threshold above which events are unambiguously detected.

$$\epsilon_{\mathrm{PC}} = \int_t^{\infty} \mathrm{PHD}(x)\mathrm{d}x = e^{-t/g}. \tag{3}$$

If we expand the exponential and solve for the minimum gain required to amplify events above a threshold t with efficiency ϵ_{PC} then we find

$$g > t/(1-\epsilon_{\mathrm{PC}}). \tag{4}$$

Therefore with a typical read noise of 100 electrons, the 5σ threshold would be $t = 500$ electrons, which could be exceeded with 90% (ϵ_{PC}) probability with a gain greater than 5000×.[16] A reasonable rule of thumb would be to operate the EMCCD with a ratio of gain/read noise greater than 50 to maximize throughput in photon counting mode.

3.2 *Coincidence Losses*

All photon counting systems will at some point lose track of incident light due to photon arrival times too close to distinguish. As discussed in the last section, the statistics of the EMCCD gain register do not allow multiple detections in a single pixel to be discriminated without added noise terms, so pixels with multiple electrons will simply be counted as one. The magnitude of this effect can be approximated by considering a 3×3 pixel region of the sensor and a frame time t s chosen long enough that on average a single pixel will be illuminated in each frame with flat field illumination. In this case the flux is $0.11/\mathrm{t}$ counts-pixel^{-1}-s^{-1}. In a period of time $2t$ s, two pixels will be illuminated in the same 3×3 frame, and 11% of the time they will be the same pixel. This means that in a frame of length t at this flux rate, 5.5% of detections will be lost due to coincidence. Following the efficiency factor definition of the last section, we define the coincidence loss efficiency factor ϵ_{CO}. For the example described

$$\epsilon_{\mathrm{CO}} = 1 - 0.055 = 0.945, \tag{5}$$

representing a small loss and justifying the rule of thumb for a photon counting system to operate at a flux of 0.1 counts-pixel^{-1}-frame^{-1} or less when possible. The coincidence loss can be generalized[17] for Poisson-distributed arrival times given a flux rate f counts-pixel^{-1}-s^{-1} and a frame time t s as follows:

$$\epsilon_{\mathrm{CO}} = (1 - e^{-ft})/(ft). \tag{6}$$

The coincidence loss efficiency factor is useful for understanding how to set the frame length for a given target. For low flux targets, it may be the case that the addition of extraneous signals such as dark current or background light should be considered in the estimation of this effect.

3.3 *Cosmic Ray Effects on EMCCD Throughput*

The EMCCD gain register is optimized for single electron input, but some bright sources in an image may not be avoidable. One example of these are cosmic rays. These energetic particles are primarily comprised of muons at sea level, and occur at a rate of about 1 cm^{-2}-min^{-1}.[18] In the Roman L2 environment, the particles are primarily protons (~74%) with energies greater than 100 MeV[11] and rates predicted to be up to 300 times higher than at sea level on Earth, or 5 cm^{-2}-s^{-1}.[19] The particles are sufficiently energetic that they are effectively unshielded by even a heavy camera housing, and each produces hundreds of electrons spread over a handful of pixels in the thin CCD. This amount of charge is not compatible with the EMCCD gain register, because it is multiplied beyond the capacity of the gain register pixels. The effect is to overspill the pixel boundaries in the serial direction, and to fill the pixel wells to the point that the charge interacts with the surface. Traps at the surface oxide are filled in this scenario and leave a trail of charge behind each cosmic ray that can be hundreds of pixels long. The detrapped charge can itself be amplified by the remaining register pixels, forming additional discreet events on top of an exponential tail. For the purpose of estimating the impact of these cosmic ray tails, we collected a series of long integrations with a commercial CCD201 EMCCD at a range of gain from 2500 to 7700 as shown in Fig. 3. It is apparent that at the gain needed for photon counting, the rate of cosmic rays at L2 presents a motivation to keep individual photon counted frames as short as possible (counterbalanced by a preference for long frames to minimize CIC). For the commercial CCD201 at a gain of 5000, the contamination of individual frames by cosmic rays would be in the neighborhood of 30% for 120 s long individual frames.

We define the efficiency factor ϵ_{CR} to account for signal pollution by cosmic ray tails as follows:

$$\epsilon_{\mathrm{CR}} = 1 - R * t * p/n, \tag{7}$$

where R is the cosmic ray rate, t is the frame time, p is the number of pixels contaminated by each cosmic ray, and n is the number of pixels in 1 cm^2 (= 591716). For an expected rate R of 5 cm^{-2}-s^{-1}, an exposure time t of 120 s, a signal pollution p of 300 pixels per cosmic ray,

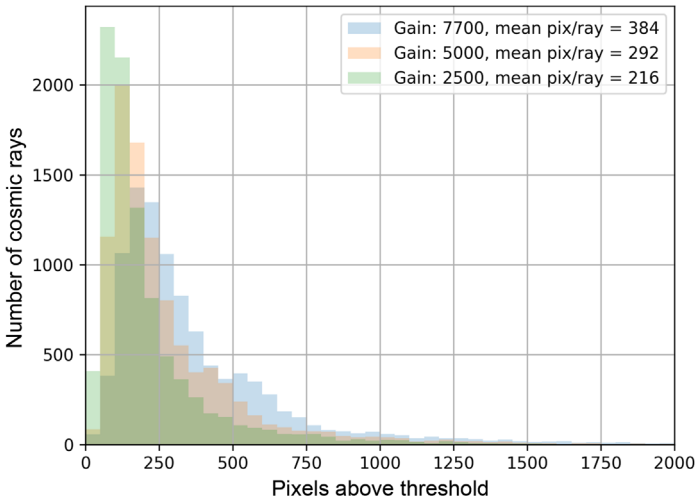

Fig. 3 The distribution of cosmic ray tail contamination (number of pixels above the five sigma photon counting threshold) versus gain for the commercial CCD201.

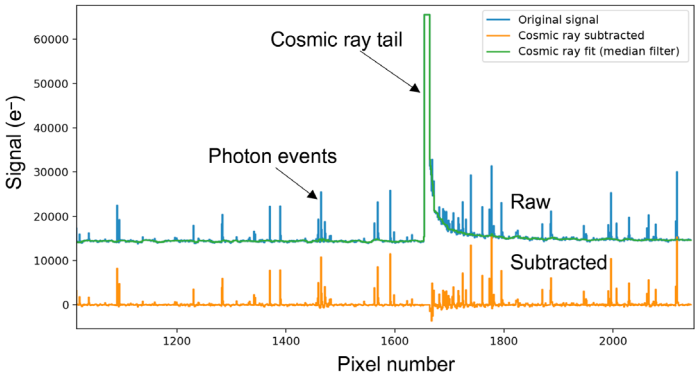

Fig. 4 The blue traces show a row of raw photon data with a representative cosmic ray tail. The green trace shows a fit to the tail generated by a median filter. The orange trace shows the fit-subtracted data, revealing an excess of events in the underlying pixels.

we find a cosmic ray efficiency factor $\epsilon_{CR} = 0.7$. Reduction of the required frame time or the number of polluted pixels per cosmic ray both result in improvements in the cosmic ray efficiency factor, and will be discussed further with respect to the improved flight design in Sec. 4.5.

The tails of the cosmic rays are reasonably fit with an exponential function that includes short and long time constants; however, as shown in Fig. 4, we have had good success simply subtracting a median filtered row from each line of data, which subtracts much of the cosmic ray tail but leaves the sharply defined photon events behind. An analysis of this data reveals that the cosmic ray tail itself can lead to additional apparent photon events by releasing electrons into the gain register that mix in with real photoelectrons. Figure 5 shows a comparison of the residual event rate in regions where tails have been subtracted to the rest of the detector. We have determined that the cosmic ray tail increases the noise significantly in the underlying pixels, and therefore it is best to eliminate the tails by other means if possible (either by shortening the frame time or optimizing the hardware).

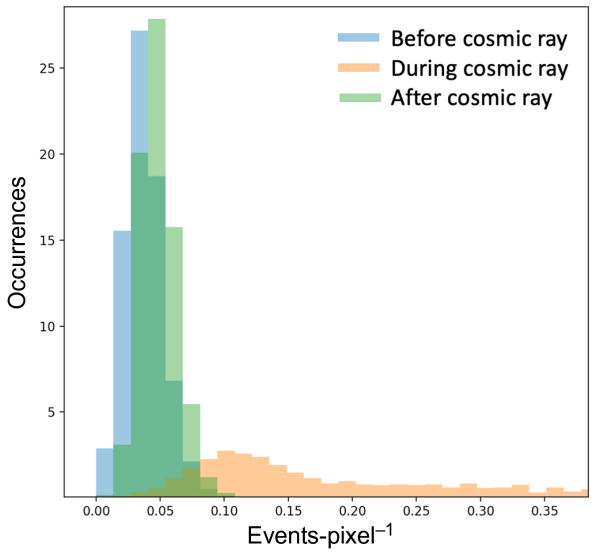

Fig. 5 A comparison of noise in image row pixels with cosmic rays before the cosmic ray is detected (blue), underneath the tail (orange), and after the tail has faded (green). These reveal that the cosmic ray tails enhance the background significantly even in regions hundreds of pixels after the cosmic ray is detected.

3.4 *Radiation-Induced Traps*

Energetic protons from flares passing through the detector will displace silicon atoms and create damage with a variety of typical forms.[20–22] Depending on the type of defect, the result will be a "trap" capable of capturing a single electron and holding it for a period of time dependent on the operating temperature. These traps reveal themselves in conventional damaged-CCD images either as elevated dark current (in the form of discreet "hot pixels"), or as "tails" behind the direction of charge transfer. The traps have an attractive charge when they are empty, and a neutral charge when full. It is typical[23] to add some charge to the image (a "flash" or "fat zero") in order to neutralize the traps and to improve charge transfer; however, the fat zero adds shot noise, defeating its purpose for a photon counting application. Furthermore, photon counting is sensitive to the impact of long time constant traps, which collect charge during readout but hold onto it long enough that it does not reappear until the next image (or longer). In this case the charge is lost and the most significant effect on the detector is to reduce its dQE, rather than to degrade the image quality since image tails typically have a very low SNR and may not be detectable.

We have characterized this effect in radiation damaged CCD301 test sensors. A line image was projected near the top row of a detector through a neutral density filter (typically ND5 or 10^{-5} transmission). We measured the ratio of the image brightness with and without the filter (a measurement of the filter transmission) as a function of the source intensity. Measurements without the filter achieve high SNR in seconds at unity gain, while measurements with the filter may take up to 100 hrs in photon counting mode. The commercial detector measurements reveal that as the brightness decreases, so does the apparent dQE when the sensor has been exposed to proton radiation. Furthermore, we found that lengthening the individual frame time had a strong effect on the faint light images, driving CGI to baseline the longest possible frames allowed by the observed cosmic ray tail length (~120 s). We interpret that in the faintest illumination conditions the detector traps are mainly empty. When the source is weak and there is no background, a significant fraction of the charge can be captured before the readout. The ratio of the measured filter transmission in faint light to the measured transmission in bright light is taken as a proxy for the charge collection efficiency factor, ϵ_{CC}.

The final efficiency factor relates to so-called "hot pixels," which are those with increased dark current as a result of radiation damage. Similar to the experience documented for Hubble Space Telescope detectors,[23] we find that a distribution of high dark current pixels develops with radiation exposure, and for CGI ~5% of pixels fail the dark current requirements after exposure to the tested level. Our approach is to mask the hot pixels, which can be considered a reduction in the detector area. In aggregate this impacts the dQE with a factor we refer to as $\epsilon_{HP} \sim 0.95$.

4 EMCCD Technology Development Program

The performance of the radiation-damaged commercial CCD201 has been reported previously for a design life of 6 years.[2] The key findings were given below.

- Devices remained functional with EM gain after a proton radiation of 2.5×10^9 p-cm^{-2} (10 MeV equivalent).
- Dark current increased by 2*x*.
- Low signal (~8 electron) charge transfer inefficiency (CTI) degraded by 5*x*.

As discussed in Sec. 3.4, further study with very low signal level imaging (e.g., photon counting with a detector-limited background) demonstrated that observed CTI degradation would manifest itself as a degradation of dQE in the form of reciprocity failure. Sufficiently faint signals would not be detected with a radiation-damaged sensor because of a population of traps available to capture the signal electrons during readout. Efforts to reduce the added dark current of damaged sensors by cooling exacerbate the CTI degradation by increasing the length of time before trapped charge is reemitted. A commonly observed consequence is the appearance of tails behind image pixels.[24] Less well known is a significant population of "*E*-center" traps[25] with time constants long enough to cause charge to be lost into subsequent frames, where it could re-appear in

any pixel of the image column. Such displaced charge is effectively lost, and is what is accounted for by the charge collection efficiency factor ϵ_{CC} described in this paper.

To address the observed radiation lifetime limitation of the commercial EMCCD, JPL funded a program at Teledyne-e2v in collaboration with CEI to develop EMCCDs with test features intended to improve performance in the space environment. We identified three key areas for improvement.

- Mitigation of traps in the image area of the sensor.
- Reduction of cosmic ray tails.
- Reduction of the required number of charge transfers to read an image.

With these things in mind, we designed two sensors, the CCD301 and CCD302, to test modifications that could improve performance in space. The elements that were implemented are summarized in Table 3, while a graphical depiction is shown in Fig. 6.

Table 3 Design feature comparison of commercial and test EMCCDs.

Parameter	CCD201	CCD301	CCD302
Light shield	Yes	No	No
Image pixel	Commercial	Multiple	Notch
Serial pixel	Commercial	Commercial	Commercial
Gain overspill	No	No	Yes
Output amplifier	Commercial	Commercial	Low noise

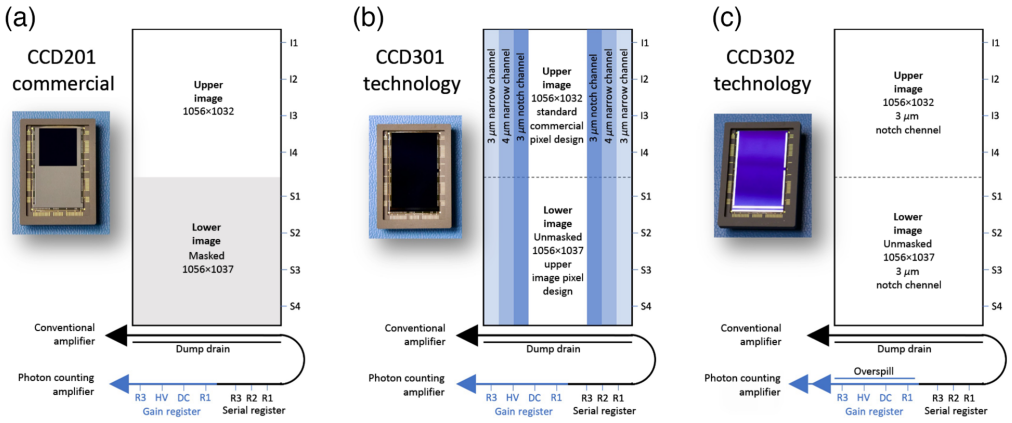

Fig. 6 (a) The commercial CCD201 consists of two similarly sized, independently clocked image sections. The design is intended for frame store operation during which the unmasked upper array can be quickly transferred to the lower one (~1 ms), which can then be read at the nominal 10 MHz pixel rate (~100 ms) while the upper image integrates the next frame. (b) The CCD301 technology program sensor eliminates the lower image frame store mask to reduce parallel transfers, and adds three new image pixel designs (highlighted in blue) intended to improve small signal charge transfer. The commercial pixel design is retained in the center as a control. The serial register and output amplifier are of the commercial design. (c) The CCD302 technology program sensor eliminates the lower image frame store mask and implements a single notch design for all image pixels. The notch design used on the CCD302 is the same as the notch design used on the CCD301. The CCD302 output amplifier utilizes an additional transistor for lower noise operation, and a gain register "overspill" feature was implemented to limit charge packets in the gain register to 100,000 electrons.

The simplest change we considered was the elimination of the store shield in the lower half of the array. This commercial sensor feature, which enables integration in the photosensitive area while the store is being read, is not necessary for the CGI applications. In the case of the ExCam, integrations are preferentially longer (up to 120 s) to minimize CIC noise and to mitigate trap damage by adding a small amount of dark current to each frame. For the LoCam, it is preferable to place the image as close as possible to the serial register to minimize latency in the wavefront sensing data. For both camera applications, the reduction of over 1000 parallel charge transfers (and >1 cm of silicon path length) reduces the exposure of signal charge to trap damage and therefore would be expected to improve charge transfer performance of damaged sensors. Rather than the "image" and "store" sections of the commercial sensor, the CCD301 and CCD302 have an "upper image" and a "lower image" that are independently clocked. The ExCam and LoCam applications only utilize the lower image section in operation.

The CCD301 included several test modifications to the image area pixel doping profiles, which affect the shape of the field inside each pixel. The nominal 13 micron photosensitive pixel width remained unchanged in each design, but the modified field would cause signal charge, especially in small parcels, to reside preferentially in a channel much smaller than it would normally have access to in the commercial sensor as it was read from the sensor. Because displacement damage due to energetic radiation occurs randomly throughout the volume of the pixel, charge that is confined in this way would be exposed to fewer possible trapping sites. We implemented four image pixel designs in seven bands across the CCD301. The bands were oriented so that half could be shielded during irradiation to provide direct before and after comparison. We studied "narrow pixel" buried channel designs intended to confine all signal charge to a fraction of the pixel area and a "notch pixel" design that modifies the commercial 9 micron buried channel with a 3 micron central well where smaller charge packets (<1000 electrons) are confined while still accommodating larger amounts of charge throughout the pixel volume. The notch concept has heritage in Hubble Space Telescope sensors[23] and has the advantage of improving performance for small signal packets while retaining most of the device full well. The central CCD301 band is the commercial control design, while bands containing progressively more aggressive modification were implemented toward the edge as shown in Fig. 6. Design 1 is a 3 micron "narrow" channel, design 2 is a 4 micron narrow channel, design 3 is a 3 micron "notch" modification to the standard pixel, and design 4 is the commercial CCD201 design.

The CCD302 was designed to study improvements to the gain register and output stage. It employed a single 3 micron notch design (the same design as implemented on the CCD301) in the image pixels and added an overspill register parallel to the gain register designed to skim off charge in excess of 100,000 electrons (the commercial design has a serial full well of >400,000 electrons). The overspill was intended to prevent cosmic ray tracks from filling the gain register corrupting the underlying signal. The CCD302 also incorporated a low noise output amplifier with an additional transistor designed to permit reduced-gain operation while maintaining a high photon counting efficiency factor, ϵ_{PC}. Reduction of cosmic ray tails is desirable to enable increased frame times in photon counting operation, both decreasing the CIC noise contribution and potentially providing additional mitigation of trap damage with the introduction of additional dark current in each frame.

4.1 *Proton Irradiation*

The expected mission dose of radiation into the silicon detectors was initially modeled for an L2 orbit and a 1 cm tantalum alloy radiation shield using a NOVICE (Experimental and Mathematical Physics Consultants, Gaithersburg, Maryland, United States) software simulation. Tantalum had been selected in the preliminary design phase but was later changed to a slightly denser tungsten alloy HD17 (17 versus 16.7 g-cm^{-3}) due to its availability. The shielding capability of the two materials is nearly identical as a result. The modeled dose is primarily protons, and includes the contribution from both solar and galactic sources. Without shielding, the galactic component would be negligible relative to the solar one. Inside the heavily shielded CGI camera, the relative contribution of GCR is enhanced to about 7% of the total because the shield does not reduce their number. The NOVICE code modeled the spatial and energy distributions through a preliminary three-dimensional mechanical model of the camera radiation

Table 4 Target radiation dosage at L2 through a 1-cm tantalum shield including an RDF of 2.

Exposure (y)	TID (rad, Si)	DDD (MeV/g, Si)
1.75	344	8.60×10^6
5.25	1033	2.58×10^7

shield and detector. Uncertainties in the transport model were accounted for by increasing the modeled dose by a "radiation design factor" (RDF) of two.

When evaluating radiation damage in the detector, both the total ionizing dose (TID) and displacement damage dose (DDD) are computed. The ionizing dose can result in trapped charge in the detector oxides, causing offsets in the required operating voltages. The displacement dose causes damage to the silicon lattice itself and creates traps for signal electrons during charge transfer. Sometimes these are caused by different types of particles with different energy spectra, but in the case of the CGI at L2, the model assumes the same protons cause both effects. The TID impact on the EMCCD was evaluated previously by CEI[26] and found to be small, 0.14 V-krad^{-1}. The results of the NOVICE simulation provided the target dosages for the test campaign shown in Table 4. Because the protons result mainly from solar flares, and since a large fraction of the total dose may come from a small number of flare events, it is important to recognize that a significant amount of granularity is possible in the time to reach a given dose level. For test purposes, the results represent the dose that will not be exceeded with 95% confidence during a goal 5.25-year mission lifetime.

Input particles were assumed to be isotropically distributed and have an energy spectrum based on measured solar flare characteristics. To determine the optimal proton energy for the test campaign, we weighted the energy distribution of protons arriving at the detector by the "non-ionizing energy loss" factor,[27] which represents the relative amount of energy absorbed by the silicon as a function of incident proton energy. The weighted mean of this function provided the "damage weighted energy" of ~85 MeV that we used in our test. Note that protons lose a significant amount of energy traversing the shield, so the source particles outside the shield would be closer to 150 MeV and on the high energy tail of the solar flare.

We irradiated CCD301 and CCD302 test sensors at James M. Slater MD Proton Treatment and Research Center, Loma Linda University Medical Center (Loma Linda, California, United States). The sensors were each installed on a support bracket as shown in Fig. 7. Each sensor was shielded by a 15-mm-thick stainless steel shield over the control half of the detector, while the bare portion (which included the serial register) was exposed to the proton beam. The sensors were irradiated in an unbiased, room temperature condition. The "5 year" dose of 85 MeV protons applied to the unshielded half of the detector was 7.4×10^9 protons-cm^{-2} (corresponding to a DDD of 2.4×10^7 MeV/g and a TID of 790 Rads). The reported displacement damage dose scales to 2.6×10^9 protons-cm^{-2} "10 MeV equivalent."[28] As the shield design has matured, predictions for the 5.25 year, 85 MeV lifetime dose have fallen significantly and therefore we expect the current results are conservative, particularly with consideration of the required 21-month instrument lifetime.

4.2 *Test Equipment*

The majority of the undamaged sensor characterization was performed at the Centre for Electronic Imaging of the Open University under contract to JPL. CEI utilized an XCam (Northampton, UK) XCU-A 1 MHz programmable CCD controller with a custom vacuum cryostat interfaced to a Polycold (Petaluma, CA) Cryotiger cooling system shown in Fig. 8. An x-ray fluorescence tube with a Mn target was housed inside the vacuum to provide charge transfer calibrations similarly to an ^{55}Fe technique. Measurements were performed at −105°C. The CEI tests emphasized performance characteristics, such as full well, dark current, and the CCD302 custom amplifier glow, which were not expected to be significantly impacted by the difference in readout speed from the flight 10 MHz implementation.

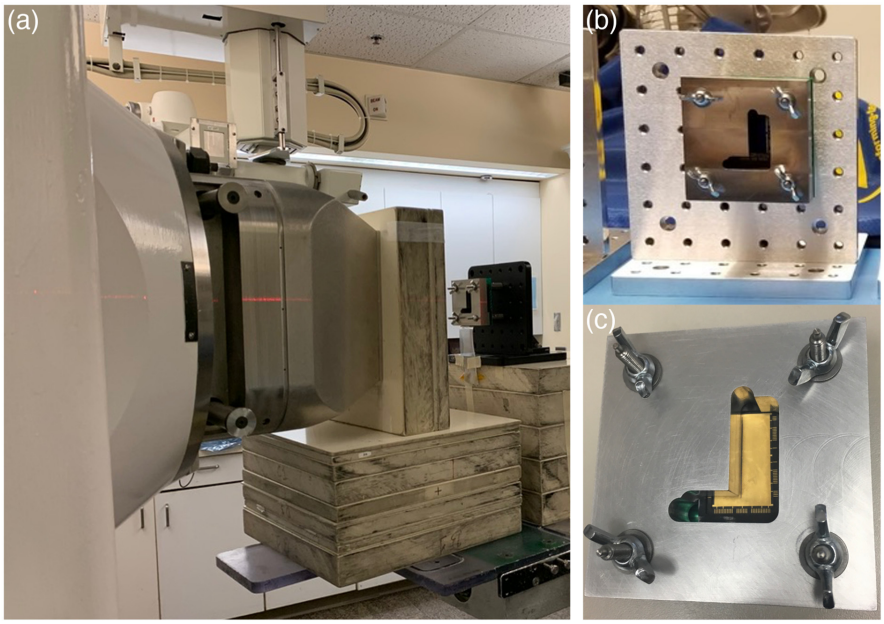

Fig. 7 (a) The proton irradiation test configuration at Loma Linda Medical Center. (b) A close-up of the EMCCD and test shield. (c) A test package behind the shield (without silicon) revealing the unshielded half of the package.

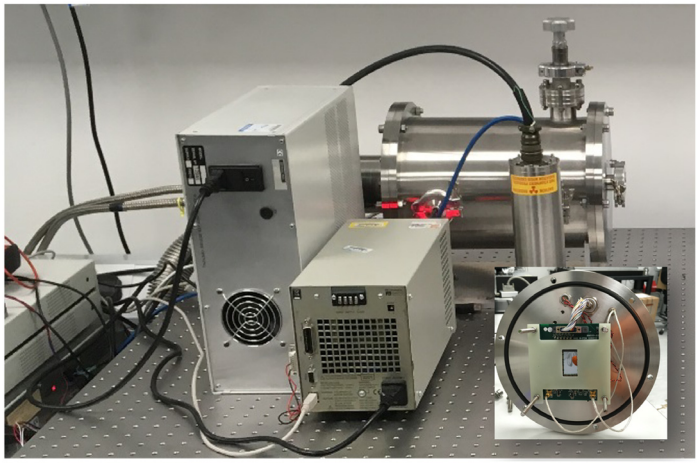

Fig. 8 The CEI test camera utilizes a 1 MHz XCam XCU-A programmable controller coupled to a custom vacuum cryostat. The headboard and CCD, cooled by a Polycold Cryotiger to −105°C, is shown in the inset. An x-ray source is incorporated inside the vacuum for use in charge transfer calibration.

The post-irradiation characterization campaign was conducted at JPL. The system, which is shown in Fig. 9, consisted of a NuVu Cameras (Montreal, California, United States) liquid nitrogen cooled EMN2 camera driven by a CCD Controller for Counting Photons (CCCP)[16] modified to adapt the entrance aperture to the unmasked design of the test sensors. The typical CCD operating temperature was −105°C. The JPL tests emphasized measurements of quantities that were expected to be significantly impacted by the flight-design 10-MHz pixel rate. These included the low flux, photon counting mode performance as well as measurements of CIC and read noise. The low flux tests provided a measurement of the relative performance of the CCD301 image pixel designs, where the inclusion of the commercial pixel provided for an overall normalization of results. JPL testing included cross-checks of some of the CEI-measured parameters, such as photon transfer to ensure consistency between the two sets of results.

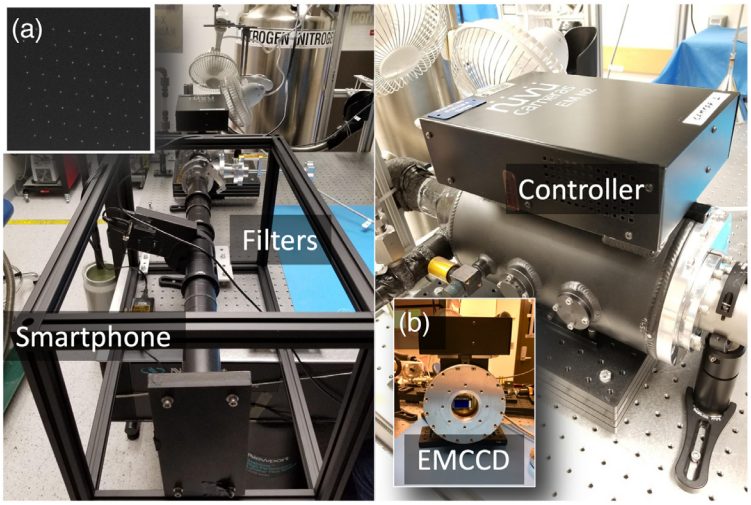

Fig. 9 (a) A view of the smartphone projector system used for EMCCD characterization at JPL. Inset of panel A shows an example image from the projector. (b) The JPL test camera utilizes a 10-MHz NuVu CCCP programmable controller coupled to a custom vacuum dewar and is cooled by liquid nitrogen to −105°C. Inset of panel B shows a test EMCCD in the commercial dewar.

The CEI and JPL test equipment made use of a smartphone-based projection system[29] that enables RGB illumination with a spatial resolution similar to the capability of the EMCCD. Because the phone has an organic light-emitting diode (OLED) screen, it provides very low leakage into parts of the field that are turned off. A filter wheel adds neutral density filters that enable a wide range of flux conditions suitable for simulating the expected illumination conditions.

4.3 *Preirradiation Characterizations*

4.3.1 *Photon transfer*

The full well characteristics of the four image pixel designs and the serial register of the CCD301 were evaluated with a standard photon transfer technique[30] using flat-field illumination. The transfer curve of each design region of the sensor was evaluated separately and the result is shown in Fig. 10. As expected, the standard commercial pixel has the highest full well since the features in the other designs reduce the width of the signal channel.

We also evaluated the full well of the serial register (identical to the commercial CCD201) by binning charge from multiple image rows at each line transfer. The image full well results are

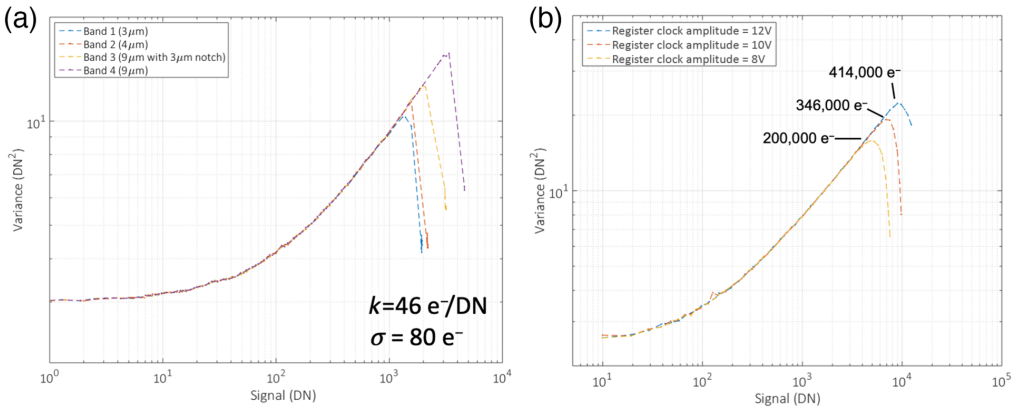

Fig. 10 (a) Photon transfer curves from CEI in the 1 MHz camera for each of the four image pixel designs contained in the CCD301 test sensor. (b) Photon transfer curves for the CCD301 register, which is common to all of the image pixel designs, at three clock voltages.

Table 5 CCD301 image full well versus clock voltage.

Voltage	3 micron	4 micron	Notch	Commercial
(V)	(Electrons)	(Electrons)	(Electrons)	(Electrons)
10	32,000	35,000	58,000	79,000
11	34,000	40,000	62,000	84,000
12	36,000	42,000	62,000	89,000

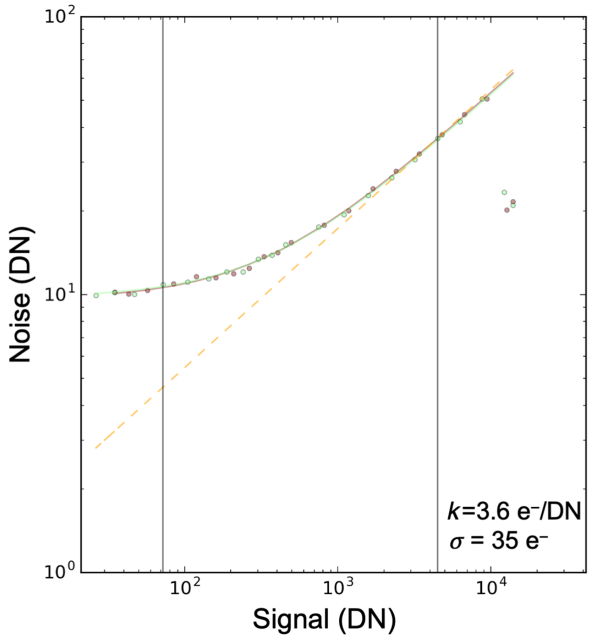

Fig. 11 A photon transfer curve for the CCD302 in the JPL 10 MHz camera.

presented in Table 5. It can be seen that the notch and commercial image pixel designs meet the 50,000 electron image and 90,000 electron serial full well requirements with margin.

For comparison, a photon transfer curve of a CCD302 (with the "notch" image pixel design) that was taken with the test camera at JPL at 10 MHz is shown in Fig. 11. The CCD302 devices included an extra transistor in their output amplifiers intended to improve the read noise performance, and were successful in this regard, achieving 35 electrons at 10 MHz.

While the CCD302 exhibited excellent read noise, it was found that the amplifier glowed significantly due to the additional transistor. An example of this effect is shown in Fig. 12. The 10-s image was taken at a gain of 1500 in dark conditions and at an operating temperature of −105°C. The amplifier glow is seen to originate in the corner closest to the output amplifier, and to extend across the entire image area. In the image shown the glow is ∼100 times higher than the dark current. We found that the glow could be mitigated by reducing the output amplifier drain voltages; however, this also caused the read noise to increase and it was deemed too risky to proceed to flight with the CCD302 amplifier design given the importance of low dark current to CGI.

4.3.2 *Gain register overspill*

We evaluated the CCD302 gain register overspill feature by comparing the responses of the CCD301 and CCD302 gain registers in photon counting mode to single bright pixel events using

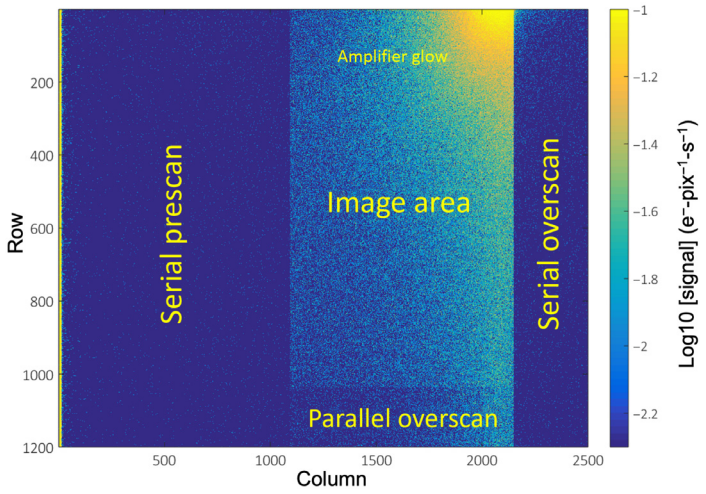

Fig. 12 A 10-s CCD302 image with gain set to 1500 shows glow from the corner of the imager close to the amplifier extending across the entire photosensitive area.

a technique developed by CEI. Simulated cosmic rays were created by collecting a flat field image and erasing all of the pixels but one into the serial register dump gate and associated conventional amplifier sense node. A high gain image was then read out through the photon counting (LS) amplifier in such a way that 500 empty rows were clocked before and after the single bright pixel. An example of an image with a simulated cosmic ray constructed in this manner is shown in the inset of Fig. 13. Since the CCD302 has a lower noise amplifier than the CCD301, the gain and threshold that would be selected for photon counting are both lower than for the CCD301, which has a register and output amplifier that are identical to the commercial CCD201. Figure 13 compares the number of photon events detected 6000 pixels after the bright pulse with the CCD301 at a gain of 4000× (with a read noise of 80 electrons and a counting threshold of 400 electrons) to the same quantity with a CCD302 at a gain of

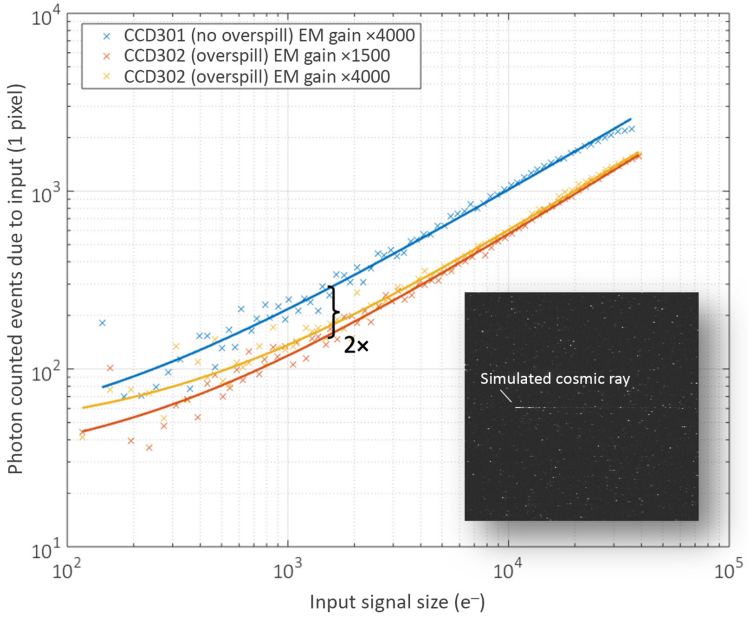

Fig. 13 A comparison of the CCD301 and CCD302 register response to a single bright input pixel in photon counting mode. The figure shows the number of pixels after the bright pulse that would be counted as photons above the counting threshold. The inset shows an example "simulated cosmic ray," which is the result of a single bright pixel pulse to the gain register operating at high gain. Trailing pixels result from trapped charge at the register surface oxide due to the amplified signal.

1500× (with a read noise of 30 electrons and a counting threshold of 150 electrons). We also measured the CCD302 pulse-response performance at the same gain and threshold as the CCD301 to explore the possibility of a systematic. Our results show that the overspill reduces the quantity of spurious detected events after a bright pixel pulse through the gain register by at least a factor of two. We also found the same result with the CCD302 in the low and high gain configurations, confirming the improvement in performance with this feature.

4.3.3 *LoCam lifetime*

While the ExCam is designed to look at the faintest objects that are detectable, the LoCam is designed to look at some of the brightest, with fluxes high enough to fill the pixel in a 1-ms frame interval. It is well known that the EMCCD gain register is susceptible to an "aging" effect in which operation with both high fluxes and gain can degrade the response of the register and in extreme cases cause it to fail. The effect is thought to be the result of charge being trapped in the oxide of the gain register, causing a flat band shift of the voltage (personal communication, P. Jerram). To study this effect, we framed a CCD301 (without an overspill) continuously with flat field illumination of 10000 electrons-pixel^{-1}-frame^{-1} at a gain of 25 (~37 V HV) as shown in Figure 14. This configuration in the 1 MHz camera achieved a charge input to the gain register of 2×10^{14} electrons after 24 hours, and resulted in a linear decrease of 2% in the gain, which was restored with an increase of 50 mV to the HV clock without otherwise impacting performance. The camera controller has a capability of up to 50 V, although according to product literature[31] the charge transfer capability is expected to degrade after 4 to 5 volts of compensation. Since the total signal input to the gain register is estimated to be 1.9×10^{15} electrons during the 21-month technology demonstration, the LoCam is expected to meet the requirements of CGI with margin.

4.4 *Postirradiation Characterizations*

4.4.1 *Low flux results*

A 100 h low flux exposure selected from the lower image area (closest to the serial register) of an irradiated CCD301 is shown in Fig. 15. The image is comprised of 100-s frames of data, each collected at a gain of 3300× and −105°C. The 100-s frame time was selected to optimize performance following initial trials that revealed poor low flux performance with short (1 to 10 s) frames. We attribute improvements at 100 s to additional dark current ($10 - 30$ electrons-column^{-1}) in each frame that would be available to mitigate trap damage without increasing coincidence losses, while not reducing the cosmic ray efficiency factor

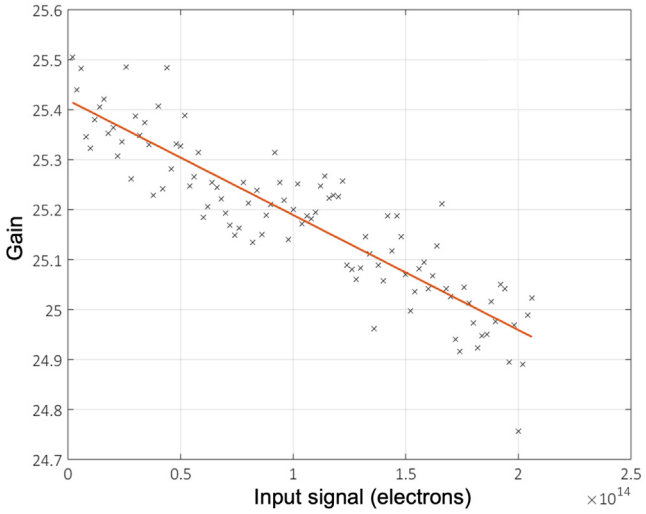

Fig. 14 Measured electron multiplying gain as a function of signal input to the gain register at a gain of 25×.

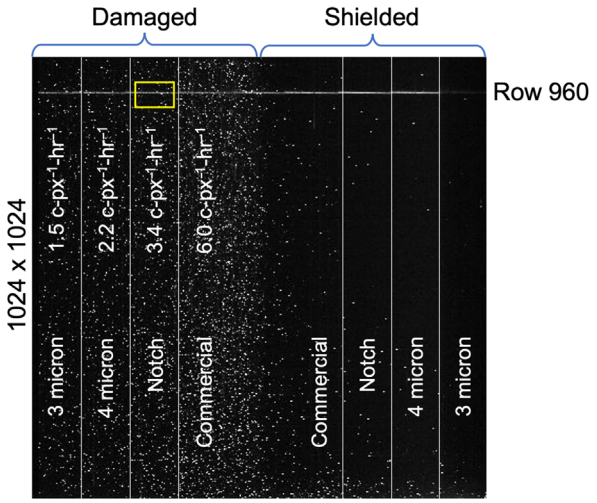

Fig. 15 A 100-hr photon counted CCD301 image comprised of 100-s frames of data. A line image from the projector illuminates row 960 near the top of the array. The pixel designs are mirror-imaged on the left and right sides of the image with the shielded right hand side providing a control. The 95% dark level measured after irradiation is overlaid on each design on the left side of the figure. The yellow rectangle shows an example extraction area for the irradiated notch-design data.

ϵ_{CR} unreasonably. At the measured gain, ~80% of events are brighter than the 5σ threshold (in this case, 693 electrons). The lefthand side of the imager as well as the serial and gain registers were irradiated, while the right hand side was protected by a shield as shown in Fig. 7. Our dataset is comprised of three image sets at different fluxes in the range of 0.001 to 0.1 counts-pixel^{-1}-s^{-1}, comparable to the stated flux requirements.

Each 100-s frame of data was bias subtracted, and photon events larger than the threshold were added to the resulting 100-hr image. The image is annotated to show the locations of the different image pixel designs, mirrored on the right and left of the sensor following Fig. 6(b). The right side annotation shows the image pixel design while the mirrored left side shows the measured dark current for 95% of the damaged pixels. Some damage (in the form of hot pixels) is also visible on the right side of the image, decreasing with distance from the center and therefore interpreted as the result of shadowing of the protons under the mask, which sat ~3 mm above the sensor during the irradiation. Detailed histograms of the measured dark in each region are shown in Fig. 16.

Near the top of Fig. 15 and annotated as "Row 960" there is a horizontal line, which is an image projected across the top of the array and used to evaluate the impact of traps on charge transfer. Close inspection reveals that the line is not perfectly uniform but rather has pixel-level structure that depends on the exact distribution of traps in a particular column. It is visually evident that the density of hot pixels is highest in the irradiated commercial-design pixels. It is also evident that the shielded 3 micron notch design on the far right has poor charge transfer. While we do not have a good explanation for this, it was observed on a number of the 3 micron test sensors and as a result that design was rejected pending further study. The 4 micron narrow channel design did not exhibit the charge transfer defect, but it also did not meet the full well requirement for CGI.

The resulting images were corrected for CIC (measured in a row overscan region above the image area), and the mean of the middle 68% of pixels for each row was computed within each design band (100 columns) for a 30 row section of the image centered on the projected line. We found that this "clipped mean" technique effectively removed the significant influence of hot pixels on the measurement. At the lowest fluxes, we estimate the hot pixels contributed an error of ~10% to the flux measurements, which we determined by comparing line profiles measured in different regions of each design band. An example fit is shown in Fig. 17.

This analysis was completed for bright (conventional) images of the scene with no neutral density filter, and faint (photon counted) images with the filter. An example bright light image

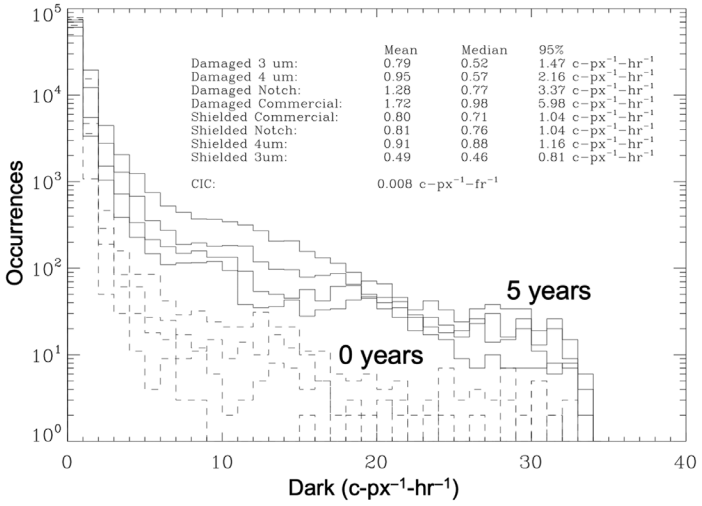

Fig. 16 Dark current histograms extracted from the photon counted image shown in Fig. 15. Each histogram is extracted from a different design region as labeled. The shielded half of the array provides the "0 year" beginning of life data while the irradiated half represents the 5-year lifetime goal at L2.

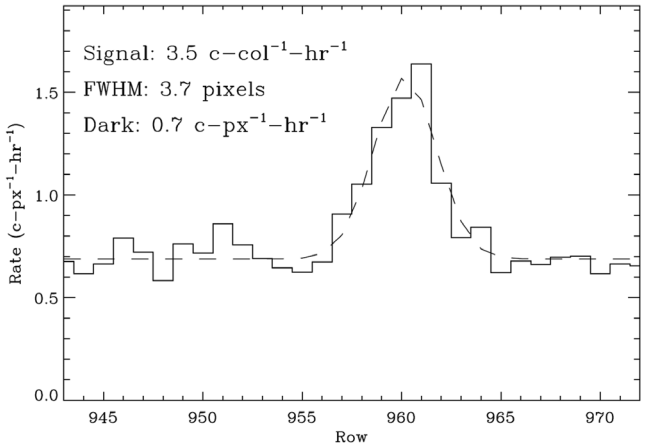

Fig. 17 The measured "clipped mean" of 100 pixels of irradiated notch-design data in each row across the projected line image shown in the yellow rectangle in Fig. 15. The dashed line represents a Gaussian fit to the measurement. The legend shows integrated signal from the fit, the full-width at half maximum (FWHM) of the Gaussian profile, and the residual dark current background.

exhibiting good uniformity (±6%) without the ND5 filter is shown in Fig. 18. To minimize systematics, a single ND5 filter was used for all of the faint light measurements while using the projector to adjust the brightness. The results were corrected for photon counting gain ϵ_{PC} and coincidence ϵ_{CO}. In Fig. 19, the ratio of the faint to bright signal is plotted against the bright light measurement scaled by the nominal 1×10^{-5} filter transmission. The ratio of the faint light to bright light measurement reveals little change over the measured flux range for the notch and 4 micron channel designs, while the commercial design shows a large decrease in performance as the flux decreases (reciprocity failure).

As a result of these pre- and postirradiation measurements, we are able to extract the relative performance of the CCD201, CCD301, and CCD302 sensors after the tested dose of radiation, and the results are provided in Table 6. The QE at 90% is taken as a nominal peak value for 600 nm from the datasheet. The coincidence, cosmic ray losses and hot pixel losses follow from Sec. 3, while the charge collection efficiency is taken from Fig. 19 for the faintest measurement. It can be seen that while improvements to the serial register that mitigate cosmic ray tails provide

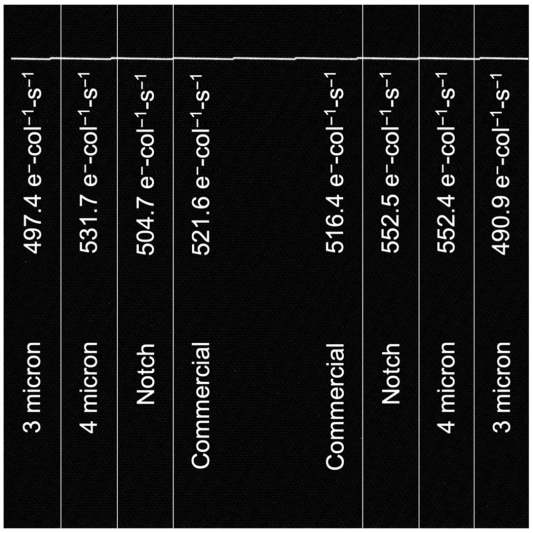

Fig. 18 An unfiltered bright light image exhibiting ±6% uniformity when comparing measured brightness in the damaged and undamaged regions. The step discontinuities are due to a small misalignment of the OLED projector to the EMCCD.

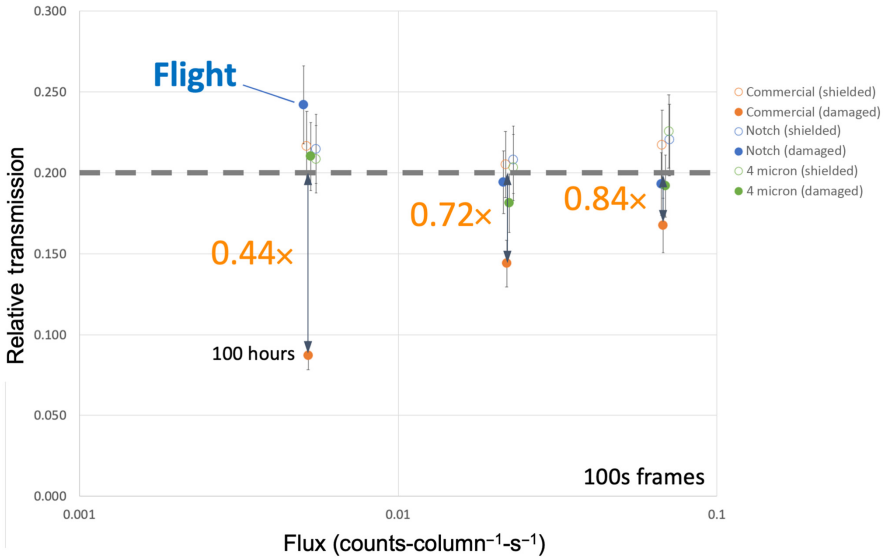

Fig. 19 A comparison of the measured projected line brightness in photon counting mode (with ND5 filter) to the brightness measured without the filter at unity gain for the 4 micron, notch, and commercial designs. The estimated flux is measured from the bright-light images (minimally affected by irradiation) scaled by 10^{-5}. The data show that the commercial design has significantly reduced faint-light sensitivity compared to the notch and 4 micron designs after it is damaged by radiation.

incremental benefits, the notch channel in the image section of the CCD301 has a large impact on performance in faint light conditions.

4.5 *Flight Sensor Design*

The CCD311 flight EMCCD has been fabricated by Teledyne-e2v through a contribution by ESA to NASA. Features from both the CCD301 and CCD302 are incorporated into the flight design for maximum improvement. Flight sensors have been delivered and are being tested at JPL. The key design elements are listed in Table 7. To simplify implementation, the CCD311

Table 6 End-of-life comparison of commercial and test EMCCD dQE performance.

	CCD201	CCD301	CCD302[a]
QE (%)	90	90	90
ϵ_{PC}	0.90	0.90	0.90
ϵ_{CO}	0.95	0.95	0.95
ϵ_{CR}	0.70	0.70	0.85
ϵ_{CC}	0.44	1.00	1.00
ϵ_{HP}	0.95	0.95	0.95
dQE (%)	22.5	51.2	62.1

[a]CCD302 amplifier glow prevented the use of long integrations with gain. CCD302 performance in this table is based on CCD301 notch channel imaging combined with CCD302 serial channel cosmic ray measurements.

Table 7 Design features of the Roman CGI flight CCD311.

Parameter	CCD311
Light shield	No
Image pixel	Notch
Serial pixel	Commercial
Gain overspill	Yes
Output amplifier	Commercial

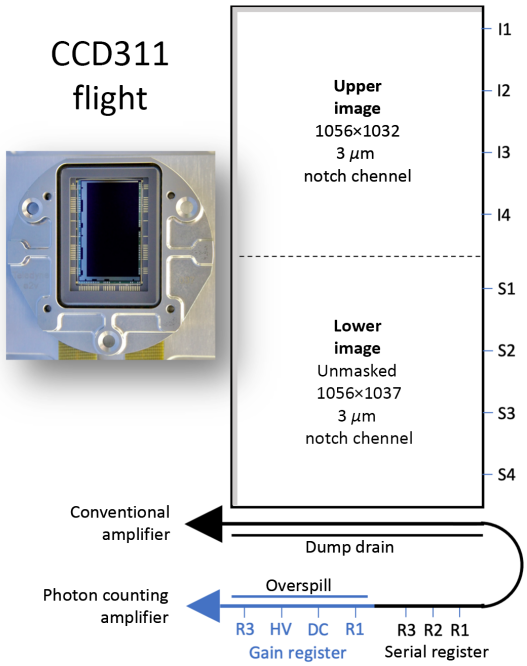

Fig. 20 The flight CCD311 EMCCD incorporates the image pixel notch feature from the CCD301 and the gain register overspill from the CCD302. It utilizes a commercial aluminum nitride carrier bonded into a nickel-plated invar package. The CCD311 is pin compatible with the commercial CCD201.

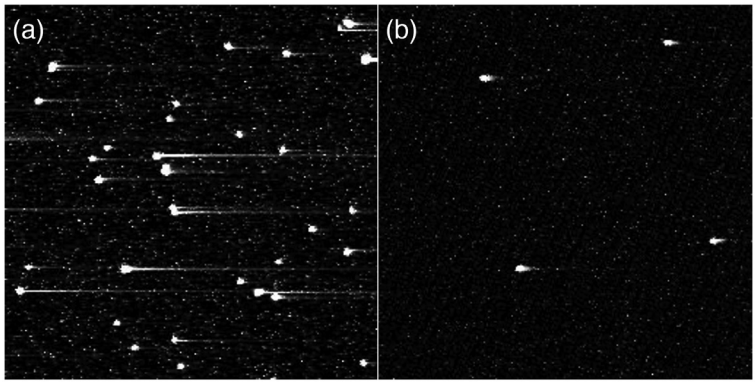

Fig. 21 A comparison of cosmic ray tails observed in the lab with the camera operating at high gain (>1000×). (a) A 256 × 256 image section from the CCD201 and (b) the CCD311 under similar conditions. The operating temperature was −105°C. The improvement is quite significant with tails in the commercial sensor example of over 100 pixels and only 40 pixels in the flight design as a result of the overspill.

uses the commercial aluminum nitride carrier and is pin-compatible with the CCD201. To provide a ruggedized thermal-mechanical interface, the aluminum nitride carrier is bonded into a nickel-plated invar package, as shown in Fig. 20.

Characterization and environmental testing of the CCD311 is underway. Early results indicate the gain register overspill is very effective at eliminating tails from cosmic rays as shown in the comparison in Fig. 21. The improvement in this key performance metric should enable the flight camera to be operated with proportionately longer frames before cosmic rays significantly obscure the image, further mitigating low signal charge transfer traps in addition to the benefit gained from the notch channel.

5 Summary

We have evaluated the impact of radiation on the low flux photon counting performance of the CCD201 commercial EMCCD and found that the design is impacted by proton exposures of a kilorad or less. We have engaged with CEI and Teledyne-e2v to model and implement targeted test features with potential to significantly improve low flux performance. The resulting CCD301 and CCD302 test sensors were irradiated with protons to the dose expected inside of our tungsten alloy radiation shield after 5 years based on software transport models. The test sensors individually exhibit low flux performance after irradiation that is improved by over

Table 8 A comparison of commercial and flight EMCCD dQE performance.

	CCD201	CCD201	CCD311	CCD311
	BOL	EOL	BOL	EOL
QE (%)	90	90	90	90
ϵ_{PC}	0.90	0.90	0.90	0.90
ϵ_{CO}	0.95	0.95	0.95	0.95
ϵ_{CR}	0.70	0.70	0.96	0.96
ϵ_{CC}	1	0.44	1	1
ϵ_{HP}	1	0.95	1	0.95
dQE (%)	53.8	22.5	73.9	70.2

a factor of two compared to the commercial design. As a result, we have selected features from them that are incorporated into the flight CCD311 design. These include an exposed lower image area modified by a 3 micron notch implant to confine small charge packets, and an overspill register parallel to the gain register to mitigate the effects of cosmic rays.

The relative performance of the commercial and flight sensor designs is shown in Table 8. The comparison is made for the faintest measured fluxes at an operating temperature of −105°C assuming the cosmic ray rate anticipated at L2 with minimal loss due to coincidence. The table constructs the expected CCD311 flight sensor performance from the measured CCD301 and CCD302 performance reported in this paper. Because the flight design combines features from both test sensors, it achieves an improvement of over a factor of three compared the the commercial design after irradiation. Results are relevant for the 100-s frame times employed for these measurements, and would be expected to degrade with shorter frame times, since residual dark current is a component of the trap damage mitigation. Preliminary results with the CCD311 are consistent with these models and will be reported in a future publication.

Acknowledgments

This research was carried out at the JPL, California Institute of Technology, under a contract with the National Aeronautics and Space Administration (Grant No. 80NM0018D0004).

References

1. B. Mennesson et al., "The Roman Space Telescope coronagraph technology demonstration: current status and relevance to future missions," *Proc. SPIE* **12180**, 121801W (2022).
2. L. K. Harding et al., "Technology Advancement of the CCD201-20 EMCCD for the WFIRST coronagraph instrument: sensor characterization and radiation damage," *J. Astron. Telesc. Instrum. Syst.* **2**(1), 011007 (2015).
3. P. Jerram et al., "The LLLCCD: low-light imaging without the need for an intensifier," *Proc. SPIE* **4306**, 178–186 (2001).
4. C. D. Mackay et al., "Subelectron read noise at MHz pixel rates," *Proc. SPIE* **4306**, 289–298 (2001).
5. L. Dressel, *Wide Field Camera 3 Instrument Handbook, Version 13.0*, Space Telescope Science Institute, Baltimore, Maryland (2021).
6. I. Poberezhskiy et al., "Roman coronagraph instrument: engineering overview and status," *Proc. SPIE* **12180**, 121801X (2022).
7. National Academies of Sciences, *Engineering, and Medicine, Pathways to Discovery in Astronomy and Astrophysics for the 2020s*, The National Academies Press, Washington, DC (2021).
8. B. S. Gaudi et al., "The Habitable Exoplanet Observatory (HabEx) Mission Concept Study Final Report," arXiv:2001.06683 (2020).
9. The LUVOIR Team, "The LUVOIR mission concept study final report," arXiv:1912.06219 (2019).
10. W. A. Traub et al., "Science yield estimate with the wide-field infrared survey telescope coronagraph," *J. Astron. Telesc. Instrum. Syst.* **2**(1), 011020 (2016).
11. M. Tanabashi et al., "Review of particle physics," *Phys. Rev. D* **98**, 030001 (2018).
12. R. E. McGuire and T. T. von Rosenvinge, "The energy spectra of solar energetic particles," *Adv. Space Res.* **4**(2-3), 117–125 (1984).
13. J. Feynman, G. Spitale, and J. Wang, "Interplanetary proton fluence model: JPL 1991," *J. Geophys. Res.* **98**, 13281–13294 (1993).
14. A. G. Basden, C. A. Haniff, and C. D. Mackay, "Photon counting strategies with low-light-level CCDs," *Mon. Not. R. Astron. Soc.* **345**, 985–991 (2003).
15. M. S. Robbins and B. J. Hadwen, "The noise performance of electron multiplying charge-coupled devices," *IEEE Trans. Electron Devices* **50**, 1227–1232 (2003).
16. O. Daigle et al., "Extreme faint flux imaging with an EMCCD," *PASP* **121**, 866–884 (2009).

17. J. L. A. Fordham, C. F. Moorhead, and R. F. Galbraith, "Dynamic-range limitations of intensified CCD photon-counting detectors," *Mon. Not. R. Astron. Soc.* **312**, 83–88 (2000).
18. D. Groom, "Cosmic rays and other nonsense in astronomical CCD imagers," *Exp. Astron.* **14**, 45–55 (2002).
19. W. Viehmann et al., "Photomultiplier window materials under electron irradiation: fluorescence and phosphorescence," *Appl. Opt.* **14**(9), 2104–2115 (1975).
20. G. R. Hopkinson, C. J. Dale, and P. W. Marshall, "Proton effects in charge-coupled devices," *IEEE Trans. Nucl. Sci.* **43**, 614–627 (1996).
21. T. Hardy, R. Murowinski, and M. J. Dean, "Charge transfer efficiency in proton damaged CCDs," *IEEE Trans. Nucl. Sci.* **45**, 154–163 (1998).
22. J. R. Srour and J. W. Palko, "Displacement damage effects in irradiated semiconductor devices," *IEEE Trans. Nucl. Sci.* **60**, 1740–1766 (2013).
23. S. M. Baggett et al., "HST/WFC3: understanding and mitigating radiation damage effects in the CCD detectors," *Proc. SPIE* **9904**, 99045D (2016).
24. R. Massey et al., "Pixel-based correction for charge transfer inefficiency in the Hubble Space Telescope Advanced Camera for Surveys," *Mon. Not. R. Astron. Soc.* **401**, 371–384 (2010).
25. D. J. Hall et al., "Studying defects in the silicon lattice using CCDs," *J. Instrum.* **9**, C12004 (2014).
26. N. Bush et al., "The impact of radiation damage on photon counting with an EMCCD for the WFIRST-AFTA coronagraph," *Proc. SPIE* **9605**, 96050E (2015).
27. I. Jun et al., "Proton nonionizing energy loss (NIEL) for device applications," *IEEE Trans. Nucl. Sci.* **50**(6), 1924–1928 (2003).
28. B. Jun, "High energy proton radiation test design for coronagraph CCD camera," in *JPL Interoffice Memorandum, 5132-18-023*, Jet Propulsion Laboratory (2019).
29. M. Bottom et al., "Smartphone scene generator for efficient characterization of visible imaging detectors," *Proc. SPIE* **10709**, 107092R (2018).
30. J. Janesick, K. Klaasen, and T. Elliott, "CCD charge collection efficiency and the photon transfer technique," *Proc. SPIE* **0570**, 7–19 (1985).
31. e2v Technologies, Ltd., "Low light technical note 5: an overview of the ageing characteristics of L3Vision sensors," tech. rep., e2v Technologies, Ltd., Chelmsford, UK (2006).

Patrick Morrissey is a physicist specializing in the development of instrumentation for astronomy at the NASA Jet Propulsion Laboratory. Currently, he is working as a delivery manager for the Roman Coronagraph camera systems described in this paper. He has previously been coinvestigator at the NASA GALEX UV sky survey, and the project scientist and optical designer for the Keck Cosmic Web Imager Integral Field Spectrograph currently operating on Maunakea, Hawaii.

Leon Harding received his PhD in astrophysics with instrumentation from the University of Galway in Ireland. Currently, he is working as a research associate professor at the Virginia Tech National Security Institute and as the assistant director of the Mission Systems Division. He leads teams in space technology development and pursues research in stellar/planetary magnetic activity and planetary exploration. Prior to VT, he was a working as a technologist at Jet Propulsion Laboratory and a scientist at Caltech.

Nathan Bush is working as a technologist at the NASA Jet Propulsion Laboratory working on the flight implementation of EMCCDs for the Roman Coronagraph Instrument. Prior to this, he was working as a research fellow at the Centre for Electronic Imaging, Open University, United Kingdom. He has contributed significantly to the development of custom sensors for space-based astronomy missions and developed novel techniques for the characterization of radiation damaged sensors.

Michael Bottom is working as an assistant astronomer at the University of Hawaii Institute for Astronomy. He works in the field of high-contrast imaging and also has experience with radial velocity exoplanet instrumentation. Previously to joining the faculty of the IfA, he was an optical engineer at JPL, working on developing the WFIRST coronagraph camera and formation flying

sensors for the Starshade mission. His research interests are the detection and characterization of extrasolar planets.

Bijan Nemati received his PhD in high energy physics from the University of Washington in 1990. Since 2001, he has been working on modeling and technology development of advanced space-based astronomical instruments, such as interferometers and coronagraphs, first at Jet Propulsion Laboratory and recently at Tellus1 Scientific, a company he founded. On the Roman coronagraph, he has served as modeling lead and system engineer for detectors and the overall coronagraph error budget.

Richard Demers is working as the manager of the Wavefront Sensing and Control Group at GMTO Corporation. He has over 30 years of experience in the aerospace and tech industries specializing in optical, sensing, and laser engineering. He was working as a program manager at GM Cruise in the development of LIDAR. He contributed to NASA missions, such as the Roman Space Telescope as assistant instrument manager of the coronagraph instrument.

Biographies of the other authors are not available.